PAPER

Swelling as a stabilizing mechanism in irradiated thin films: II. Effect of swelling rate

IOP Publishing Journal of Physics: Condensed Matter
J. Phys.: Condens. Matter **34** (2022) 325302 (18pp) https://doi.org/10.1088/1361-648X/ac75a3

Swelling as a stabilizing mechanism in irradiated thin films: II. Effect of swelling rate

Tyler Evans* and **Scott Norris**

Department of Mathematics, Southern Methodist University, Dallas, TX 75275, United States of America

E-mail: tylere@smu.edu

Received 19 May 2022
Accepted for publication 1 June 2022
Published 15 June 2022

Abstract

It has long been observed experimentally that energetic ion-beam irradiation of semiconductor surfaces may lead to spontaneous nanopattern formation. For most ion/target/energy combinations, the patterns appear when the angle of incidence exceeds a critical angle, and the models commonly employed to understand this phenomenon exhibit the same behavioral transition. However, under certain conditions, patterns do not appear for any angle of incidence, suggesting an important mismatch between experiment and theory. Previous work by our group (Swenson and Norris 2018 *J. Phys.: Condens. Matter* **30** 304003) proposed a model incorporating radiation-induced swelling, which is known to occur experimentally, and found that in the analytically-tractable limit of small swelling rates, this effect is stabilizing at all angles of incidence, which may explain the observed suppression of ripples. However, at that time, it was not clear how the proposed model would scale with increased swelling rate. In the present work, we generalize that analysis to the case of arbitrary swelling rates. Using a numerical approach, we find that the stabilization effect persists for arbitrarily large swelling rates, and maintains a stability profile largely similar to that of the small swelling case. Our findings strongly support the inclusion of a swelling mechanism in models of pattern formation under ion beam irradiation, and suggest that the simpler small-swelling limit is an adequate approximation for the full mechanism. They also highlight the need for more—and more detailed—experimental measurements of material stresses during pattern formation.

Keywords: numerical, stability, ion-beam, sputtering, swelling, irradiated, isotropic

(Some figures may appear in colour only in the online journal)

1. Introduction

The manufacture of complex nanostructures is of interest for a variety of potential applications, including the production of novel materials, medical devices and semiconductors. Since at least the 1960s, spontaneous nanoscale pattern formation has been observed on surfaces subject to ion bombardment in the 100 eV–10 keV range, with resulting patterns including ripples [1]; hexagonal arrays of dots on the scale of 5–20 nm [2]; and continuous transitions there-between [3]. The use of ion beam irradiation to induce pattern formation is of particular interest because ion beam technology is already widely available in industrial settings, and so a rigorous theory of irradiation-induced pattern formation could enable the rapid, inexpensive and well-controlled mass-production of various useful nano- and meta-materials. An ideal model of this process would determine all relevant factors and the relationships between them to the extent that experimental results can be reliably predicted to high precision. Control could then be exerted over the system dynamics to enable fine-tuned

* Author to whom any correspondence should be addressed.

nanoscale manufacture, sometimes referred to as 'bottom-up' micromachining: that is, by designing manufacturing processes that operate coarsely at scales potentially much larger than the nanometer-sized structures that result from the process. However, despite widespread interest spanning many decades [4], the general theory is far from complete.

Despite the lack of an overarching theory, some things have been well-established. For instance, it is understood that the bottoms of troughs may erode faster than the tops of peaks, generating an instability [5–8], and that the orientation and wavelength of the resulting surface ripples can depend not only on the angle of incidence of the ion beam, but also its energy. Separately, atoms displaced but not sputtered away by an ion impact have also been shown to significantly affect surface stability [9–12]; these complementary erosive and redistributive effects have more recently been integrated through the crater function framework approach [13–17]. In addition to these so-called 'prompt-regime' effects associated with individual ion impacts, a number of mechanisms operate in the 'gradual regime' over much longer time scales. In particular, accumulated radiation damage leads to the amorphization of a thin film of near-surface material, which can be modeled as a highly viscous fluid subject to surface energy effects [18]. Finally, within this film, significant stresses are created during irradiation [19–23], and material-dependent responses to these stresses can also contribute to pattern formation [24–28]. The relevance of numerous effects operating at various scales contributes to the difficulty of the development of a precise understanding of the formation of these nanostructures [29, 30].

In recent years, many ion-induced nanopatterning experiments have been conducted on Si (due to its relevance to the semiconductor industry) at irradiation energies of 1 keV or below (due to the ready availability of ion guns designed for this energy range). For this material at these energies, it is observed that as the ion-incidence angle θ increases from 0° (normal incidence) to 90° (grazing incidence), the patterns formed transition from flat surfaces, to ripples with wave vector parallel to the ion beam, to ripples with wave vector perpendicular to the ion beam, and that these transitions occur independently of ion energy [31–33]. Most of the theoretical models described in the previous paragraph exhibit similar behavior. Importantly, however, this behavior does not seem to be universal, and some researchers have reported a complete absence of patterns for some ion/target/energy combinations—we are motivated in particular by the experiments of (a) Teichmann *et al* [34], who observed no patterns at any studied angle for $Ne^+ \rightarrow Ge$ or $Ar^+ \rightarrow Ge$ between 400 and 2000 eV, and (b) Hofsäss *et al* [35], who observed no patterns at any studied angle for $Ar^+ \rightarrow Ge$ between 2 keV and 5 keV. These observations suggest the presense of an additional, unconditionally-stabilizing mechanism that becomes important in these regions of parameter space; however, this is puzzling, as all of the many models described in the previous paragraph are destabilizing for at least some incidence angles.

Recent experimental studies have suggested that impact-induced stresses may be the single greatest contributor to the transition from smooth surfaces to ripples at an incidence of around 45 degrees and an energy near 1 keV [29]. This suggests asking whether some novel stress-related mechanism could exist that is unconditionally stable, explaining the suppression of ripple patterns discussed above. In particular, whereas existing stress-based pattern formation models have employed the convenient incompressibility condition at low energies [24, 25, 25–28], researchers have long observed radiation-induced swelling at higher energies, induced by a variety of atomistic mechanisms [36–43]. Accordingly, recent work by our group explored replacing the incompressibility condition with a simple mathematical model of isotropic swelling, and found that swelling does, indeed, supply the needed surface stabilization at all angles of incidence [44]. However, due to the mathematical complexities of the model, analytical solutions could only be obtained in the limit of very small swelling rates, whereas the observed pattern suppression would presumably occur above some critical value of the swelling rate.

In this work, we generalize the prior results to arbitrary swelling rates using new analytical and numerical approaches, closing the gap between theory and observation. After recasting the system of equations resulting from linear stability analysis to a single equation, and developing a finite difference scheme for its solution, we compute the dispersion relation at arbitrary swelling rates, wave numbers and angles of incidence. We show that the observed angle-independent stabilization is not an artifact of the small swelling rate assumption used in [44]. Indeed, we demonstrate that the overall stability structure in the full parameter space is largely independent of swelling rates despite several features unique to the nonlinear regime (including a fascinating exchange of stabilities within a multi-branch dispersion relation). With this knowledge, we then turn to several relevant experimental systems, and discuss how the presence of swelling in the model can help us to understand those observations. With this work, therefore, we have significantly strengthened the hypothesis of a needed swelling-induced stabilization mechanism, highlighting the potential importance of this effect in future work, and an urgent need for more experimental data on swelling rates.

2. Preliminaries

We will use the same model as in [44]; here we will briefly summarize that model and some preliminary results obtained from its analysis.

2.1. Model

We consider a thin, crystalline material irradiated from above by an ion beam, with the z-axis oriented normal to the surface. The accumulation of radiation damage leads to the amorphization of the top few nanometers of the target, and this amorphous thin film is described using continuum equations for viscous fluid. Our goal is to solve equations in two dimensions for velocity $\vec{v}(x,z) = u(x,z)\hat{i} + w(x,z)\hat{j}$, the density $\rho(x,z)$,

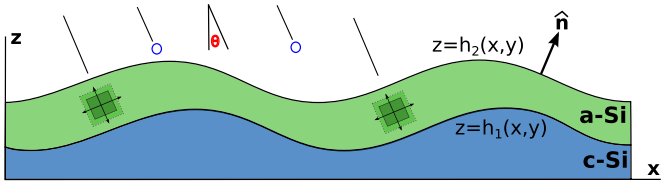

Figure 1. Schematic depicting ion bombardment at an incidence angle of θ, the resulting formation of an amorphous layer with thickness determined by the ion penetration depth, and an pictorial illustration of the proposed swelling mechanism. Note that for off-normal incidence, the bottom boundary $z = h_1(x,t)$ may not align with the top boundary $z = h_2(x,t)$.

pressure $p(x,z)$, and an age-tracking variable $a(x,z)$ within a thin film bounded above by an amorphous–vacuum boundary $z = h_2(x,t)$ and below by a crystalline–amorphous boundary $z = h_1(x,t)$. This geometry is illustrated in the schematic in figure 1.

2.1.1. Bulk equations. In the bulk, the standard equations for conservation mass and momentum, respectively, are

$$\frac{\partial \rho}{\partial t} + \nabla \cdot (\rho \vec{v}) = 0 \tag{1}$$

and

$$-\nabla p + \eta(\nabla \cdot (\nabla \vec{v}) + \nabla(\nabla \cdot \vec{v})) = 0 \tag{2}$$

where η is the viscosity, and we have used the viscous limit of Stokes flow, which is is justifiable due to the dominance of 'creep' forces over inertial forces in the bulk. We note that the density is not constant, and therefore the incompressibility condition $\nabla \cdot \vec{v}$ does not apply. As a result, we must also supply an equation of state to relate the irradiation-induced damage to the density. As a simple model appropriate to a first study, we choose the equation

$$\rho = \frac{\rho_0^*}{1 + \alpha a}, \tag{3}$$

where ρ_0^* is the original density of the crystalline solid, α is a constant expansion rate, and a is an 'age' variable that tracks the length of time a parcel of material has existed within the irradiated film, according to a simple forced advection equation

$$\frac{\partial a}{\partial t} + \vec{v} \cdot \nabla a = 1 \tag{4}$$

in which the 1 on the right hand side provides the steady increase in age as time progresses. Because equation (3) lacks a pressure term, it can be thought of as a 'quasi-incompressibility' condition—i.e. the density is allowed to change in response to changes in *age*, but not to changes in *pressure*. This preserves some of the analytical convenience of incompressibility, while allowing density changes due to irradiation.

It is worth re-emphasizing from [44] that our model of swelling is *mechanism-agnostic*. In other words, whichever specific atomistic mechanism causes the increase in volume over time (i.e. defects and accumulated damage, vacancies coalescing into voids, implanted ions forming bubbles, etc), that process appears in equation (3) only indirectly by way of the age variable. In this mathematical simplification, swelling simply proceeds linearly in time (i.e. proportional to accumulated fluence) once a parcel of material becomes amorphized at the bottom of the film, and proceeds until the parcel is removed by sputtering at the top of the film.

2.1.2. Boundary conditions. At the crystalline–amorphous (bottom) boundary $z = h_1(x,t)$, the standard no-slip and no-penetration conditions are applied simultaneously as

$$\vec{v} = \vec{0}. \tag{5}$$

At the amorphous–vacuum (top) boundary $z = h_2(x,t)$, we have the following two boundary conditions:

$$v_{\hat{n}} = \vec{v} \cdot \hat{n} - V\frac{\rho_0^*}{\rho} \tag{6}$$

and

$$[\mathbf{T}] \cdot \hat{n} = -\gamma \kappa \hat{n} \tag{7}$$

where equation (6) is a modified kinematic condition that incorporates the sputtering of material at the free interface (V is the surface sputter velocity) [44]. Finally, equation (7) is a standard conservation of momentum applied at the interface, $[\cdot]$ denotes the jump across the interface, and the stress tensor is that of a standard Newtonian fluid,

$$\mathbf{T} = -p\mathbf{I} + \eta(\nabla \vec{v} + \nabla \vec{v}^{\top}). \tag{8}$$

Because the effect of surface tension in pattern formation is well-established [18], we here take $\gamma = 0$ to focus entirely on the effect of the swelling mechanism.

2.2. Previous results

In [44], the above model is first non-dimensionalized and translated into a frame of reference moving downward with the eroding surface at speed V. (In this frame of reference, material appears to pass upward through the crystalline/amorphous boundary, proceed to swell as it rises through the film, and finally be sputtered away once it reaches the free surface.) Next, steady-state solutions are computed exhibiting reflection, rotation, and translation invariance. Finally, the non-dimensionalized governing equations are linearized about the steady-state solution in normal modes with wavenumber k, leading to the following system of linearized, single-mode equations:

$$\Sigma\rho_1 - \frac{A}{\psi^3}w_1 + \frac{1}{\psi}(iQu_1 + w_1') + \psi\rho_1' + A\frac{1}{\psi}\rho_1 = 0 \tag{9}$$

$$\Sigma a_1 + \psi a_1' + A\frac{1}{\psi}w_1 = 0 \tag{10}$$

$$\psi\rho_1 + \frac{1}{\psi}a_1 = 0 \tag{11}$$

$$-2Q^2u_1 + u_1'' + iQw_1' = iQp_1 \tag{12}$$

$$-Q^2w_1 + 2w_1'' + iQu_1' = p_1' \tag{13}$$

with the following boundary conditions at $z = 0$:

$$a_1 = -h_{11}A \tag{14}$$

$$u_1 = 0 \tag{15}$$

$$w_1 = -h_{11}A \tag{16}$$

and the following boundary conditions at $z = 1$:

$$w_1 = \Sigma h_{21} - (1+2A)\rho_1 \tag{17}$$

$$u_1' + iQw_1 = -2iQ\frac{A}{\sqrt{1+2A}}h_{21} \tag{18}$$

$$-p_1 + 2w_1' = 0. \tag{19}$$

Here and throughout this paper, $Q = kh_0$ is the dimensionless wave number of a perturbation, $\Sigma = \frac{\sigma h_0}{V}$ is the dimensionless growth rate of that perturbation, $A = \alpha h_0/V$ is the dimensionless swelling rate of the film, and $\psi = \sqrt{1+2Az}$. Physically, the parameter A quantifies the relative increase in volume of a parcel of material by the time it is sputtered away, as discussed above (i.e. $A = 0.1$ reflects an increase of 10% in the volume of a parcel of matter by the time it is sputtered away, and $A = 1$ reflects a doubling in the volume).

As discussed in [44], equations (9)–(19) are seemingly not amenable to an exact analytical solution. However, a second linearization in the small-A limit leads to solvable equations, which yield the small-A dispersion relation

$$\Sigma = \left[\left(1 - \frac{\cosh(Q) + Q\sinh(Q)}{Q^2 + \cosh^2(Q)}\right)\frac{h_{11}}{h_{21}} - \frac{Q^2}{Q^2 + \cosh^2(Q)}\right]A + O(A^2) \tag{20}$$

where h_{11} and h_{21} are the lower and upper interfaces linearized in normal modes, respectively. This dispersion relation contains a pocket of stable wavenumbers approximately between $Q = 0$ and $Q = 1.5$ for all angles of incidence. A plot of (20) at normal incidence is reproduced in figure 2(a).

Although this result holds for 'small enough' swelling rates where the second linearization $A \ll 1$ is valid, we note that if isotropic swelling is hypothesized to suppress ripple formation under some set of conditions, the swelling rate must presumably be 'large enough' to do so. This necessarily requires the consideration of larger swelling rates. We therefore now turn our attention to the problem of equations (9)–(19) for *arbitrary* values of A, with two main goals in mind: first, to develop a numerical method with which we can conduct a full modal analysis for arbitrary values of Q; and second, to study the dependence of pattern formation on the full (Q, A, θ) space and compare with the small-A results.

3. Numerical methods

In this section, we describe in detail an approach to determine the linear dispersion relation numerically for arbitrary non-dimensional swelling rates A. We will restrict our attention to the parameter range $A \in [0, 1]$, which should be sufficient to capture most physical systems, even those such as irradiated Ge that exhibit extreme amounts of volumization.

3.1. Reformulation in density

We return to the full linearized equations (9)–(19), whose dispersion relation we seek for all of (Q, A, θ) parameter space. As written, equations (9)–(19) is a system of five ordinary differential equations (ODEs) with six boundary conditions, one of which (the kinematic condition (17)) must be reserved in order to determine Σ. However, in doing this, we would have no boundary condition available for the solution of ρ_1. Indeed, the boundary conditions at $z = 1$ all involve multiple unknowns, complicating numerical solution. One remedy is to simply reduce the system into the density, which yields a single fifth-order ODE with six boundary conditions. This is readily amenable to solution by simple finite differences, and may also serve as a staging point for an exact analytical solution in the future. The dimensional reduction is performed as follows:

(a) Solve for a_1 in terms of ρ_1 in equation (11).
(b) Substitute the above result into equation (10) so that w_1 is expressed in terms of ρ_1.
(c) Substitute the expression for w_1 in terms of ρ_1 into equation (9) and solve for u_1 in terms of ρ_1.
(d) Substitute expressions for w_1 and u_1 in terms of ρ_1 into equations (12) and (13).
(e) Differentiate the new equation (12) with respect to z and multiply the new equation (13) by a factor of iQ.
(f) Set these new equations (12) and (13) equal to each other to yield the fifth-order ODE with variable coefficients.
(g) Apply the implied relationships between unknowns to the boundary conditions.

The result of these operations is the ODE in the bulk

$$\begin{aligned}&(Q^4\Sigma+2AQ^4(4\Sigma z+\psi)+A^4(16Q^4z^3\psi+\Sigma(3-4Q^2z^2)^2)+8A^3Q^2z(3Q^2z\psi+\Sigma(-3+4Q^2z^2))\\&+6A^2((-Q^2)\Sigma+2Q^4z(2\Sigma z+\psi)))\rho_1-\psi^2(((-Q^4)\psi-6A(-2Q^2\Sigma+Q^4z\psi)+A^2Q^2(48\Sigma z\\&+\psi(31-12Q^2z^2))+2A^3(Q^2z\psi(31-4Q^2z^2)+6\Sigma(1+4Q^2z^2)))\rho_1'+\psi^2(2(Q^2\Sigma+2AQ^2(2\Sigma z\\&+5\psi)+A^2(-9\Sigma+4Q^2\Sigma z^2+20Q^2z\psi))\rho_1''+(2Q^2\psi+A(-12\Sigma+8Q^2z\psi)\\&+A^2(-24\Sigma z+\psi(-63+8Q^2z^2)))\rho_1^{(3)}-\psi^2((\Sigma+2A\Sigma z+18A\psi)\rho_1^{(4)}+\psi^3\rho_1^{(5)}))=0,\end{aligned}\tag{21}$$

which we note is linear and homogeneous, along with the following boundary conditions at $z=0$:

$$Ah_{11}-\rho_1=0\tag{22}$$

$$3A^2\rho_1+6A\rho_1'+3A\rho_1\Sigma+\rho_1''+\Sigma\rho_1'=0\tag{23}$$

$$A^2h_{11}+2A\rho_1+\rho_1'+\rho_1\Sigma=0\tag{24}$$

and the following boundary conditions at $z=1$:

$$\frac{\psi^2(2A\rho_1'+\psi\rho_1\Sigma+3A\rho_1+\rho_1')}{A}-h_{21}\Sigma=0\tag{25}$$

$$\begin{aligned}&\frac{2A^2h_{21}Q^2}{\psi}+4A^2\rho_1^{(3)}+20A^2\rho_1''+\frac{2A^2\Sigma\rho_1'}{\psi}+15A^2\rho_1'+\frac{3A^2\rho_1\Sigma}{\psi}+\psi^2Q^2(2A(\rho_1'+\rho_1)+\rho_1')\\&+\psi^3Q^2\rho_1\Sigma+4A\rho_1^{(3)}+2A\psi\Sigma\rho_1''+\psi\Sigma\rho_1''+10A\rho_1''+5A\psi\Sigma\rho_1'+\frac{A\Sigma\rho_1'}{\psi}+\rho_1^{(3)}=0\end{aligned}\tag{26}$$

$$\begin{aligned}&A^3(4Q^2(6\psi\rho_1''+6(3\psi+\Sigma)\rho_1'+\rho_1(5\psi+9\Sigma))-2\psi(35\rho_1''+4(\rho_1^{(4)}+7\rho_1^{(3)}))+\Sigma(3\rho_1-2(4\rho_1^{(3)}\\&+18\rho_1''+9\rho_1')))+A^2(2Q^2(18(\psi\rho_1''+(2\psi+\Sigma)\rho_1')+\rho_1(5\psi+18\Sigma))-\psi(12\rho_1^{(4)}+56\rho_1^{(3)}\\&+35\rho_1'')-3\Sigma(4\rho_1^{(3)}+12\rho_1''+3\rho_1'))+3Q^2(\psi\rho_1''+\Sigma\rho_1')+A(9Q^2(2\psi(\rho_1''+\rho_1')+\Sigma(2\rho_1'+\rho_1))\\&-2\psi(3\rho_1^{(4)}+7\rho_1^{(3)})-\Sigma(2\rho_1^{(3)}+3\rho_1''))-\psi\rho_1^{(4)}-\rho_1^{(3)}\Sigma=0.\end{aligned}\tag{27}$$

Hence we have converted a system of five differential equations in five unknowns with six boundary conditions into a single differential equation in one unknown with six boundary conditions. Although, superficially, the form of the expressions is substantially worsened by bringing them into a single unknown, finite difference methods for a single ODE are often very convenient to write and implement.

3.2. Numerical algorithm

Mathematically, equations (21)–(27) represent an eigenvalue problem for the growth rate Σ. In cases where such equations are solvable in closed form, it is typical to reserve one boundary condition (most naturally the kinematic condition, where Σ appears upon application of the linear stability ansatz), solve the system of differential equations with the remaining boundary conditions and Σ remaining an arbitrary parameter up until the end, and then to substitute the computed solution into the reserved boundary condition to determine Σ. The parameter Σ is then known in terms of the other system parameters, possibly as an implicit function. It is this approach that we seek to recreate numerically in a least-squares sense. Accordingly, we reserve (25), the kinematic condition, from which we define

$$\Pi(\Sigma;Q,\theta,A)=\frac{\psi^2(2A\rho_1'+\psi\rho_1\Sigma+3A\rho_1+\rho_1')}{A}-h_{21}\Sigma\tag{28}$$

which is just the left side of (25), and whose Σ roots we wish to compute for a given (Q,θ) pair. In general, Σ is complex-valued, and so Π will also be complex valued. To obtain the Σ roots, we therefore seek to minimize an objective function

$$\Phi(\Sigma;Q,\theta,A)=|\Pi|^2=\mathrm{Re}[\Pi]^2+\mathrm{Im}[\Pi]^2\tag{29}$$

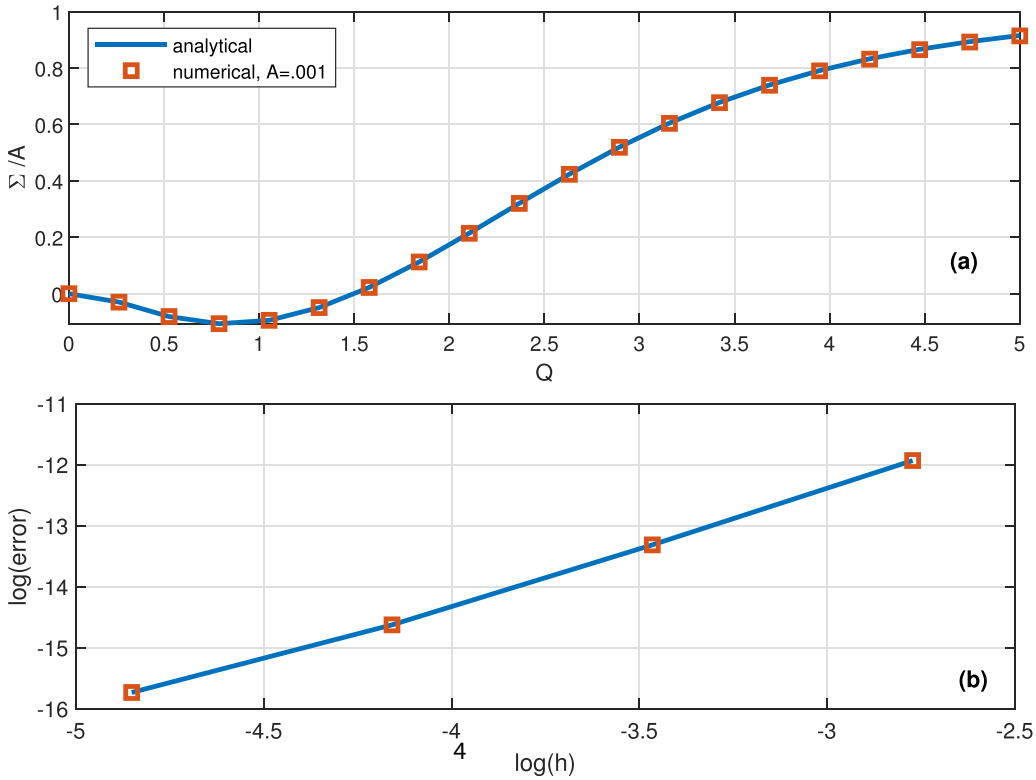

Figure 2. (a) Comparison between analytical and numerical results for small A and normal incidence. (b) Convergence analysis of our finite difference solver for $A = .2$, $Q = .7$, $\theta = 0$, using $h = \frac{1}{128}, \frac{1}{64}, \frac{1}{32}, \frac{1}{16}$ and taking $h = \frac{1}{256}$ to be the true solution. We obtain a slope of 1.9943 between values associated with $h = \frac{1}{256}$ and $h = \frac{1}{128}$ on the log–log plot, consistent with second order convergence.

which is simply the squared modulus of Π. Numerically, we designate $\Sigma(Q,\theta)$ to be a root if $\Phi(\Sigma;Q,\theta,A) < \varepsilon$. For convenience, we used Matlab's *fminsearch* function to determine the Σ roots, and our overall method may thus be summarized as follows:

(a) Set values of A,Q, θ for which we desire Σ.
(b) Set initial guess for Re[Σ] and Im[Σ].
(c) Solve BVP (21)–(27) using finite differences.
(d) Evaluate $\Phi(\Sigma;Q,\theta,A)$.
(e) **If** $|\Psi < \varepsilon|$, assign $\Sigma(Q,\theta,A)$ and **exit**
(f) **Else**, adjust Re[Σ] and Im[Σ], **go to (c)**.

In order to sweep over the minimization process, we must solve the system (21)–(27) at each iteration. We use a typical second-order central difference scheme to approximate the first through fifth order derivatives, and ghost points on each end of the domain to facilitate enforcement of the boundary conditions[1]. However, we deviate from the standard approach in an important way.

[1] 'Ghost points' are nonphysical extensions of the domain of solution which allow the application of, for example, central finite differences at boundaries where one or more of the points required for the stencil would be undefined. By considering what the value of the ghost point *would be* if the domain were continued, we can express the value at the out-of-domain grid point in terms of in-domain grid points simply by solving for them algebraically using the finite difference approximations of the boundary conditions that should apply there.

Crucially, the reservation of (25) at $z = 1$ for use as an objective function reduces the number of available ghost points at $z = 1$ from three to two, precluding the use of the typical second-order central finite difference for a fifth derivative, whose stencil involves three points on each side. Consequently, we use an off-center (but still second-order) difference scheme for the fifth derivative at $z = 1$, with weights $\frac{1}{2}, -4, \frac{25}{2}, -20, \frac{35}{2}, -8, \frac{3}{2}$ at grid points $z_{i-4}, z_{i-3}, z_{i-2}, z_{i-1}, z_i, z_{i+1}, z_{i+2}$ respectively. With our custom stencil, we require only two ghost points to the right of the interval, which are uniquely determined by the two boundary conditions at hand.

3.3. Verification and convergence

To verify the accuracy of our approach, we compare the analytical solution in the small A limit (reference) with the numerical solution for a small value of $A = .001$. In figure 2(a), we have reproduced the small-A dispersion relation from our numerical results, confirming that our combination of root-finding and finite difference methods is viable. In figure 2(b), we have conducted a convergence analysis for $Q = .7$ at $A = .2$ and normal incidence, taking mesh spacing $\Delta z = \frac{1}{256}$ to be the 'true' solution, then coarsening the mesh and recording the L^2 norm of the error between 'true' and obtained. We see a slope of approximately 2, reflecting roughly second order convergence, as expected. Other parameter choices produce similar convergence plots, giving further assurance that our method works correctly.

4. Stability results

We now use our numerical method to obtain two main sets of results. First, we obtain the full dispersion relation and relative flow fields within the film at normal incidence, and conduct a careful study of their scaling in the swelling rate A. Second, we consider the (Q,θ) dependence of both pattern growth and translation for several relevant values of A. We will demonstrate that the key results for vanishingly-small swelling rate A are reproduced for arbitrary A, while also investigating the complexities of the non-small rate.

4.1. Dispersion relation computed numerically: normal incidence

We begin with a simple depiction of the growth rates $\mathrm{Re}[\Sigma]$ in the normal incidence case. We note that, because swelling is an isotropic effect, the incidence angle appears in the governing equations only indirectly, through the relationship between the top and bottom boundaries. For normal incidence, we expect the bottom boundary to be a simple downward translation of the top boundary by a distance h_0. This means the perturbations to the bottom boundary are in phase with the perturbations to the top boundary—i.e.

$$h_{11} = h_{12}. \tag{30}$$

We also note that under normal incidence irradiation, the growth rate is purely real due to symmetry considerations.

In figure 3(a) we have numerically computed the growth rate for several values of swelling rate A ranging from $A = .01$ (1% volume increase before sputtering) to $A = 1$ (100% volume increase before sputtering). It is clear that the characteristic swelling-induced pocket of stable wave numbers below $Q = 2$ persists for all swelling rates depicted. We observe that the magnitude of the growth rate $\mathrm{Re}[\Sigma]$ increases significantly as the swelling rate A increases. This is expected, but complicates a comparison of the qualitative features of $\mathrm{Re}[\Sigma]$ for different values of A. Therefore, in figure 3(b), we scale each growth rate curve by its limiting value $C_\infty := \lim_{Q\to\infty} \Sigma(Q,A)$. The scaled curves are remarkably similar at all values of A, nearly collapsing onto the curve associated with the small-A limit. This observation, alone, significantly answers in the affirmative some of our motivating questions concerning the applicability of the small-A result in experimental settings.

Closer examination of figure 3(b) shows that the neutrally stable wavenumber Q_{neutral} is pushed slightly to the right for increasing A. Compared to its value $Q_{\mathrm{neutral}} \approx 1.508$ in the small-A limit, we observe that for $A = .1$, $Q_{\mathrm{neutral}} \approx 1.525$, and for $A = 1$, $Q_{\mathrm{neutral}} \approx 1.653$. Thus, an increased swelling rate A is seen to slightly increase the range of stable wavenumbers for normal-incidence irradiation. Finally, we observe that the roots at $Q = 0$ and Q ≈ 1.508 do not change very much for different values of A, while the curvature of the dispersion relation between these two roots appears to somehow scale by A. This prompts an exploration of the long-wave dispersion relation, and we find that, indeed, scaling by the second-derivative in Q of the arbitrary-A long-wave dispersion relation provides a good approximation (see appendix) or, equivalently, by twice the coefficient. In addition, the results of the long-wave analysis analytically confirm the angle-independent stabilization of small wavenumbers.

As a visual aid to understanding the effect of the swelling mechanism on the relative flow field within the amorphous thin film, we consider in (figure 4) a few wavenumbers for normal-incidence ion beam irradiation at both $A = .1$ (10% volume increase before sputtering) and $A = 1$ (100% volume increase before sputtering). The wavenumbers chosen are $Q \approx 0.7$, which is approximately the most stable wave number, a neutrally stable wave number depending on A, and $Q \approx 2$, a wave number which is unstable for all A that we have considered here.

It is clear from the relative flow field that for $Q = 0.7$, material tends to flow from hilltops into valleys, which has the net effect of reducing disparities between highs and lows over time. Near each respective neutrally stable wave number, vortices have begun to form which exactly balance the loss of material from hilltops with a cycling of material forced below the surface in the valleys back into the hilltops. This has the net effect of preserving the distance between hilltop and valley over time, hence neutral stability. Finally, the relative flow field for unstable wave number $Q = 2$ depicts the case where the redistribution is dominated by shear forces, with material from valleys being driven beneath the surface and then forced uphill by the sub-surface vortical flow faster than lateral expansion can compensate. This leads to growth in distance between hill-top and valley-bottom, hence instability and pattern formation.

Fundamentally, these observations are attributable to a competition between two phenomena. First, the hilltops are driven to expand laterally into valleys by the swelling mechanism. Second, shear forces tend to redistribute material vertically due to the different rate of sputtering in the hilltops and valleys, because the time until sputtering (the 'dwell time') is proportional to the depth of film relative to a given parcel of matter. For long waves, the former dominates, whereas for short waves, the latter dominates. This basic mechanism is fundamentally unchanged by different values of A. As can be seen, the proposed swelling mechanism continues to exert a robust, qualitative effect on the dispersive behavior of the medium even when A is non-vanishing. This demonstrates that the earlier findings are not attributable to the smallness of the swelling rate that was originally considered, and are representative of a real effect that is manifest at all positive swelling rates.

4.2. Exploration of full (Q,A,θ) dependence

We now turn our attention to the behavior of $\mathrm{Re}[\Sigma]$ and $\mathrm{Im}[\Sigma]$ at incidence angles other than zero. To explore the effect of off-normal incidence, we follow [28, 44] and assume that the bottom boundary is still translated a distance h_0 from the top boundary, but *in the direction of the ion beam*. Hence, by simple geometry,

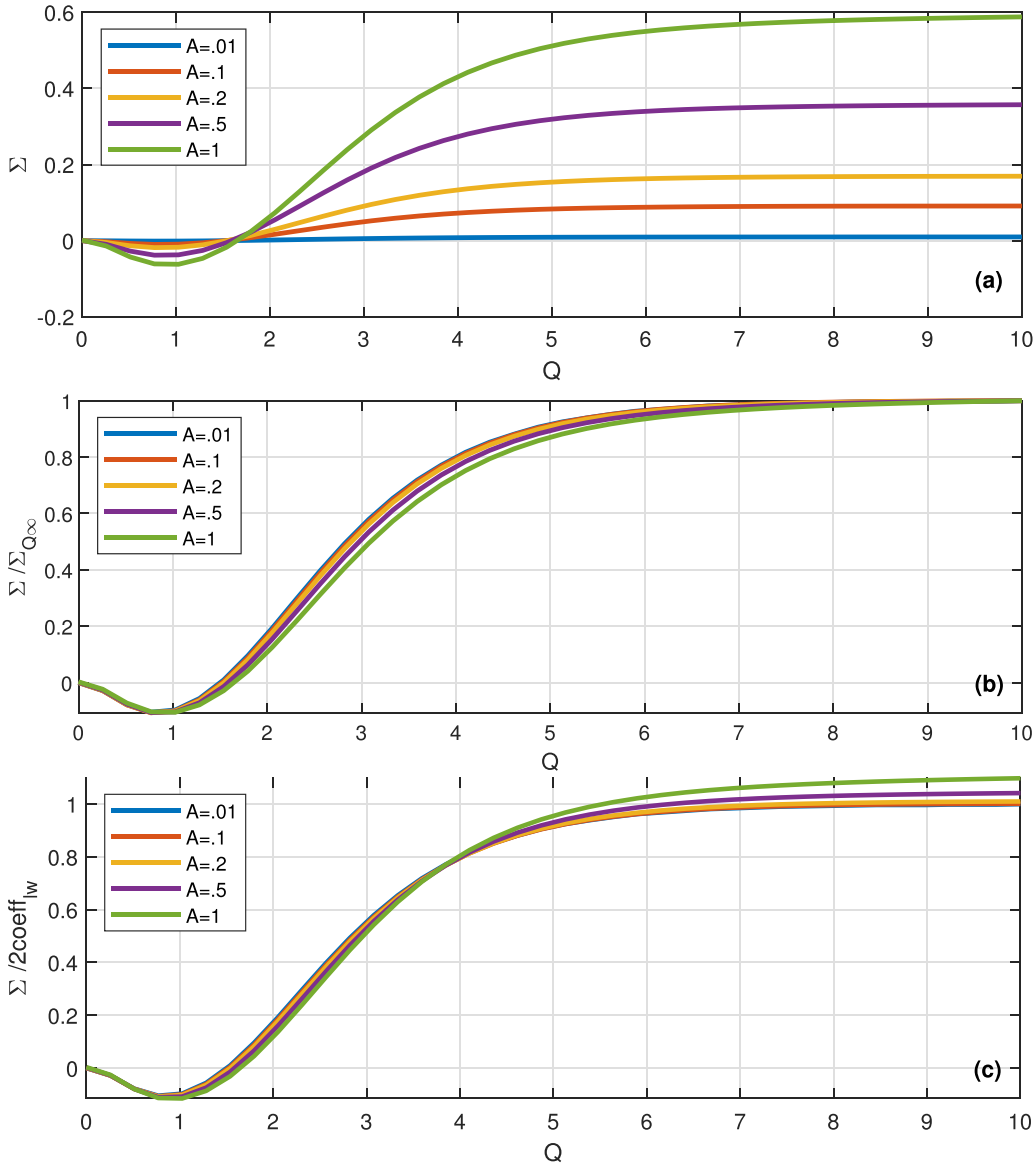

Figure 3. Dispersion relations computed numerically. (a) Unscaled, showing behavior in absolute terms. We note an apparent preservation of shape. (b) Scaled by the large-Q asymptote for each A, demonstrating that the $Q \to \infty$ limit provides a natural scaling factor. (c) Scaled by the second derivative of the long-wave coefficient.

$$h_1(x,t) = h_2(x - h_0\sin(\theta), t) - h_0\cos(\theta). \tag{31}$$

This reduces the steady film depth according to

$$h_{0\theta} = h_0\cos(\theta), \tag{32}$$

which causes a corresponding re-definition of the dimensionless wave numbers:

$$Q_\theta = Q\cos(\theta). \tag{33}$$

Finally, it also induces a phase shift in the perturbations of the top and bottom boundaries, yielding:

$$h_{11} = h_{21}e^{-iQ_\theta\tan(\theta)}. \tag{34}$$

We will consider the dependence of $\mathrm{Re}[\Sigma]$ and $\mathrm{Im}[\Sigma]$ on a range of angles between $\theta = 0°$ and $\theta = 90°$, but we will neglect the relative flow fields for these angles in favor of representing the data more broadly as two pairs of heat maps in A and θ. Recall that we are ultimately interested in the behavior of ϵ-small perturbations to a steady state: $f(x,z,t) = f_0(z) + \epsilon\tilde{f}(z)e^{\Sigma t + iQx}$. Then we have

$$f(x,z,t) = f_0(z) + \epsilon\tilde{f}(z)e^{\mathrm{Re}[\Sigma]t + iQ\left(x + \frac{\mathrm{Im}[\Sigma]t}{Q}\right)} \tag{35}$$

such that $\mathrm{Re}[\Sigma]$ is associated with growth (>0) or decay (<0) in time, and $\mathrm{Im}[\Sigma]$ is associated with translation left (>0) or right (<0) on the x-axis.

4.2.1. Real part. Comparing with the results of [44], figure 5 demonstrates that the angle dependence observed for the vanishingly-small swelling rate is reproduced at higher swelling rates with a strong analogy between each $\Sigma(Q,\theta;A)$.

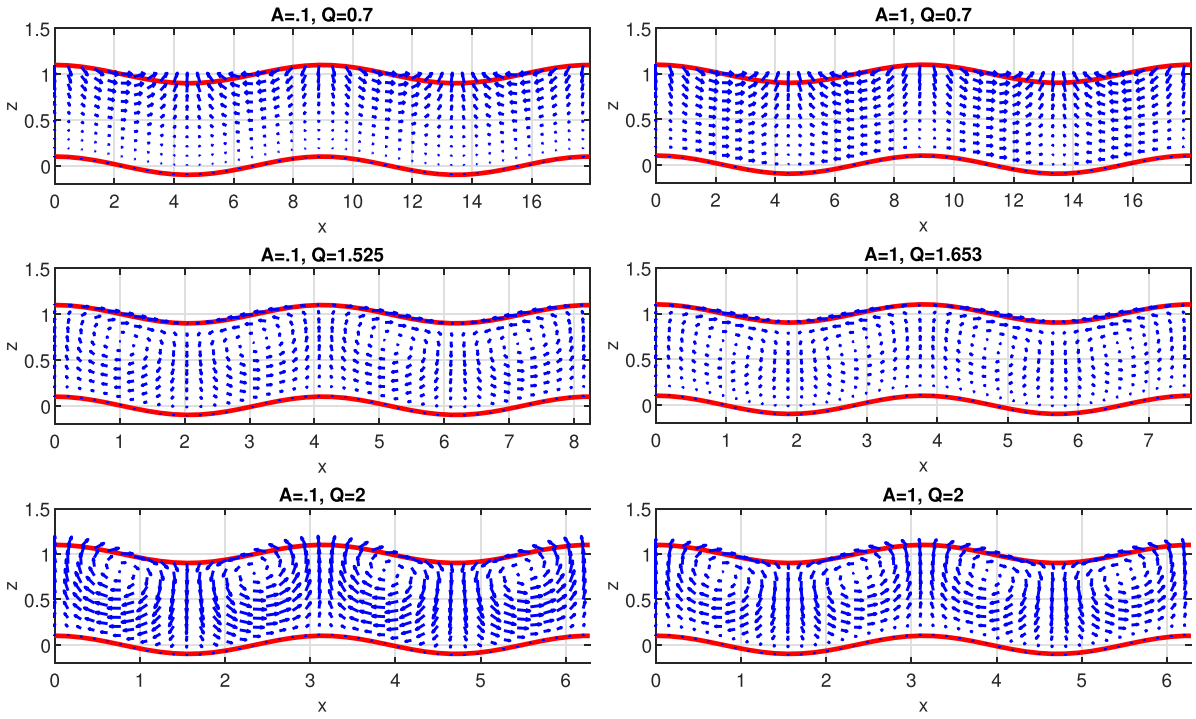

Figure 4. Comparison of relative flow fields for $A = 0.1$ versus $A = 1$. We plot the velocity fields $\vec{v}_{11}(x,z;Q) - \vec{v}_{11}(x,z;0)$ for several representative wave numbers. Subtracting off $\vec{v}_{11}(x,z;0)$ isolates the components relevant to linear stability by removing a strong, constant, downward velocity associated with the traveling frame, as in [44]. First row: lateral expansion drives the flow of material from hilltops into valleys, tending to stabilize. Second row: lateral expansion and shear forces attempting to pull material uphill are evenly matched, leading to neutral stability. Third row: shear forces have overcome the lateral expansion, pulling more flow of material uphill than can be offset by lateral expansion, leading to instability.

Comparing the first row of the heatmap (or, equivalently, figure 3) to the associated result for the $A \to 0$ limit [44], we see near perfect agreement. As A increases the general form of the real part of sigma remains unchanged, while some interesting behavior is seen in the imaginary part, which we will discuss below. This again confirms that the qualitative behavior of the swelling mechanism is not strongly dependent on the swelling rate A, further confirming the motivating hypothesis of this work.

Focusing on the real part (left-hand column), some minor dependence on A may be noted. In particular, increased A is associated with an expansion of the unstable regions in general, and a contraction of the stable regions. At the same time, the small-angle stability frontier is pushed into higher wave numbers, and the large-angle stability frontier is reduced in its extent. This is most evident at $\theta = 0$ and $\theta = 45$. For $\theta = 0$, $A = .1$ yields $Q \approx 1.525$ as first neutrally stable wave number greater than 0, whereas $A = 1$ yields $Q \approx 1.653$ as the first neutrally stable wave number greater than 0, suggesting that increased swelling rate is associated with slightly larger wave numbers becoming stable: a *stabilization* of larger wave numbers at small angle of incidence. On the other hand, for $\theta = 45$, with $A = .1$, the first non-zero neutrally stable wave number is $Q \approx 6.5$, and for $A = 1$, it is $Q \approx 6$. We also note that previous results for vanishingly-small A yield $Q \approx 7$ [44]. This effect is perhaps most evident around $\theta = 35$, where the expansion of the unstable region for smaller angles has 'cut off' a previously stable region, now *destabilizing* it. This illustrates that although the existence of a swelling mechanism always induces stability for small wave numbers, it may stabilize *or* destabilize wave numbers in the general phase space depending on A and θ.

4.2.2. Imaginary part. Turning our attention to the imaginary part of Σ, we again see marked similarity between images for different values of A, with one notable exception: the apparent replacement of some of the neutral stability regions by sudden changes in the direction of translation, which is unexpected. Indeed, investigating a 'slice' of the heat map at $\theta = 45°$ for different values of A (figure 6), we observe that, for sufficiently high A, discontinuities appear to form!

The key to understanding these *apparent* discontinuities is twofold. First, after further investigation, we notice that they occur when the upper and lower interfaces h_{11} and h_{21} are exactly out of phase, which is to say that $\frac{h_{11}}{h_{21}} = -1$. Equation (34) implies that this occurs when

$$e^{-iQ\sin(\theta)} = -1 = e^{-i(2n+1)\pi} \tag{36}$$

or explicitly, when

$$\theta = \arcsin\left(\frac{(2n+1)\pi}{Q}\right). \tag{37}$$

These curves are plotted as dashed black lines in figure 5, and it can be seen in figure 6 that the apparent discontinuities

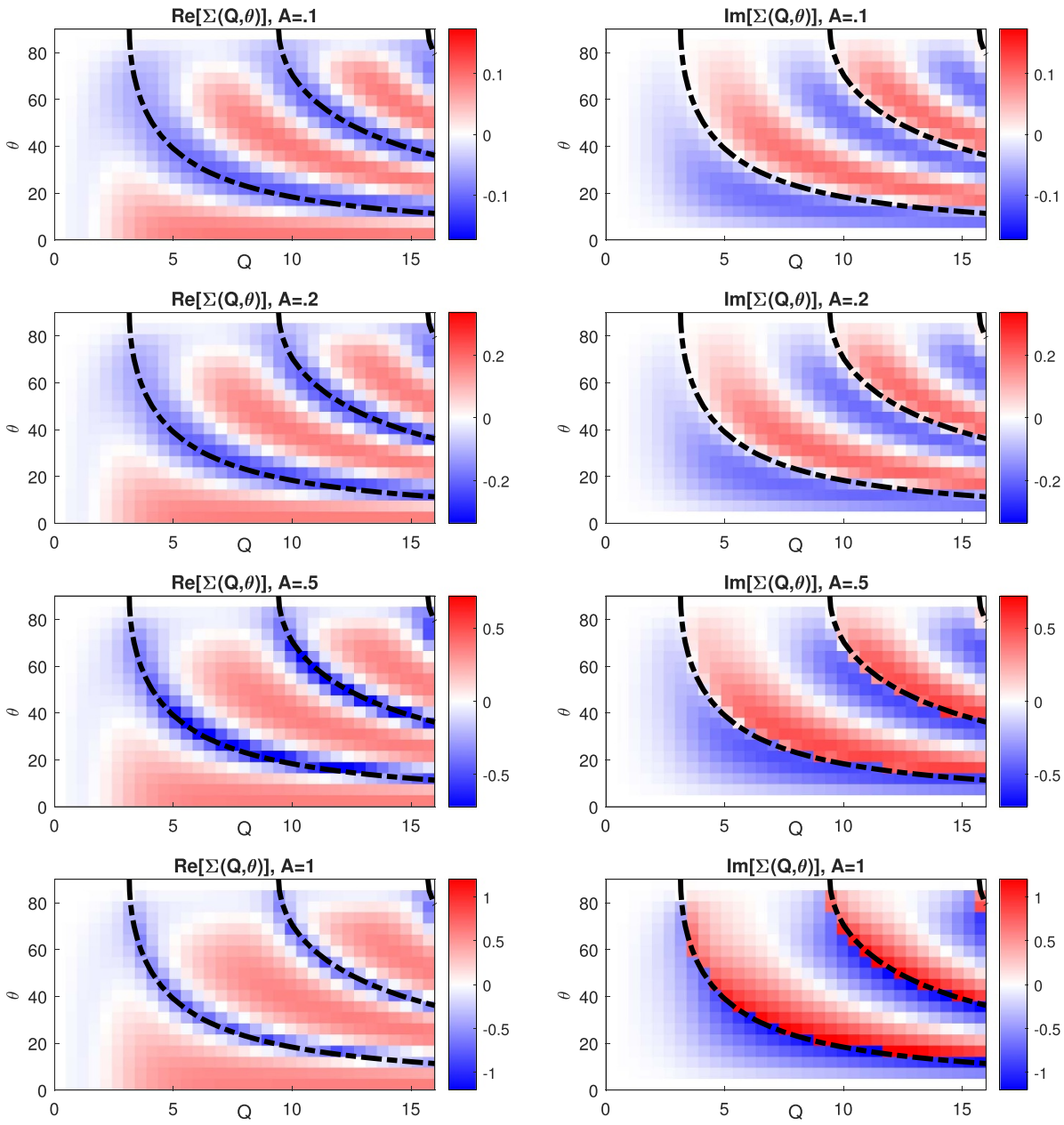

Figure 5. Comparison of heat maps for select swelling rates A. Black dashed lines show the level curves $Q\sin(\theta) = \pi, 3\pi, 5\pi$ for which the upper and lower interfaces are exactly out of phase.

lie directly upon them. Second, we must realize that the out-of-phase interface configuration exhibits left-right symmetry, such that any solution with non-zero translation rate *must have a partner solution* moving in the opposite direction with the same speed. These observations suggest that the solution for Σ contains more than one branch, and that what appear to be discontinuities in $\mathrm{Im}[\Sigma]$ may in fact simply represent an exchange of stability between branches.

With such consideration in mind, we now treat the regions around the apparent discontinuities more carefully. By adjusting the initial guesses that our numerical solver makes in minimizing the error (29), we indeed are able to obtain more than one solution branch for Σ, which are shown in figure 7.

We now see clearly that at the point of the 'discontinuity' in $\mathrm{Im}[\Sigma]$, the two branches of $\mathrm{Re}[\Sigma]$ cross. This complicates visualizations of the dispersion relation, which reflect a traditional focus of stability analyses only on the branch with the most positive value of $\mathrm{Re}[\Sigma]$. Our more careful computations reveal that this maximal value *changes branches* at a critical value of Q, resulting in the *apparent* cusps and discontinuities seen in figure 6.

It turns out that the separation of the two intersecting branches of $\mathrm{Im}[\Sigma]$ begins around $A^* \approx .55$ for $\theta = 45$. Although we have not shown it here, analogous transitions occur near $Q \approx \frac{6\pi}{\sqrt{2}}$ for $\theta = 45$, and, more broadly, near the entire level curve defined in (37) at various critical thresholds

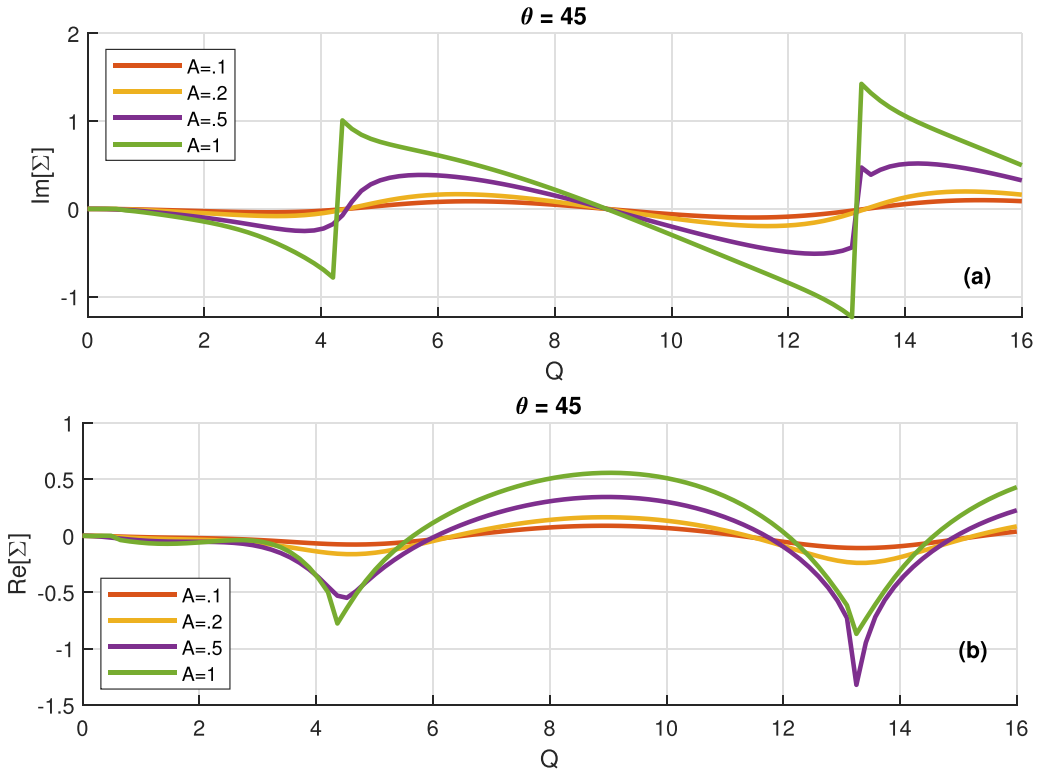

Figure 6. A slice of the heat map at $\theta = 45$, illustrating the increasingly sensitive dependence on Q as A increases.

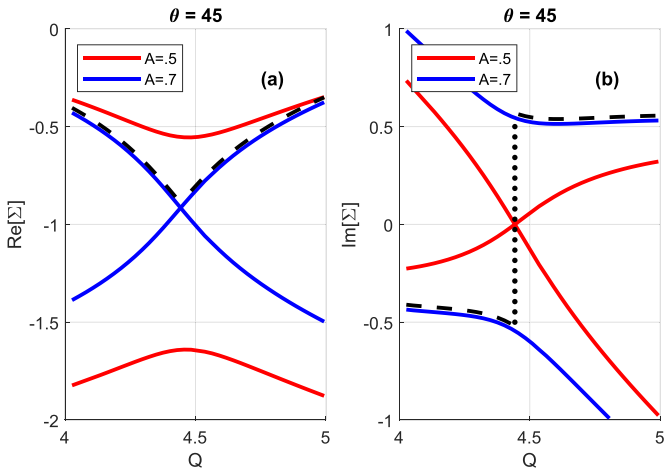

Figure 7. Transition diagram of the multi-branch structure near $Q \approx \frac{2\pi}{\sqrt{2}}$ on the out-of-phase level curve as A is toggled.

$A^*(Q,\theta)$. Thus all of the rapid transitions in figures 5 and 6 can be explained.

5. Discussion

In this section, we consider the implications of our results for the interpretation of certain experimental observations. We begin with some general observations on how the swelling mechanism should affect the pattern-forming properties of a system. It is essential to note that, as discussed in [44], swelling operates simultaneously with other, previously-studied mechanisms such as sputter erosion [5–8], mass redistribution [9–12], and anisotropic stress-driven flows [24, 25, 27, 28]. A schematic exploration of the addition of the swelling mechanism to these existing models is illustrated in figure 8. There, we see that a modest amount of swelling will be expected to increase the transition angle separating flat surfaces from rippled surfaces, whereas a large amount of swelling might be expected to suppress ripple formation entirely. A detailed attempt to estimate all relevant parameters is beyond the scope of this work, but in what follows we provide some qualitative discussion in the context of relevant experiments.

5.1. Comparison with selected experiments

5.1.1. $Ar^+ \to Si$ below 1000 eV. We first review observations in a 'reference' system of $Ar^+ \to Si$ at energies below 1000 eV, as studied by Madi *et al* [31–33]. At near-normal incidence, patterns are not observed, but above a transition angle of about 45°, ripples emerge with wavevector parallel to the ion beam direction. Finally (although this is not our focus), above a second transition angle of around 80°, these 'parallel-mode' ripples are replaced by 'perpendicular-mode' ripples with wavevector perpendicular to the ion beam. In this energy range, the transition angles are not observed to depend strongly on the ion energy. We would conclude that any swelling in this system is either present in low amounts, or does not depend strongly on the ion energy within this energy range.

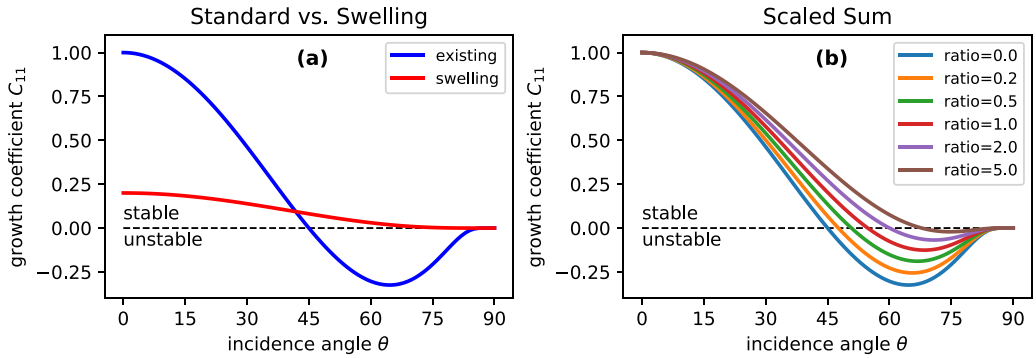

Figure 8. A schematic illustrating the expected effect of swelling on the stability coefficient C_{11}, in a longwave linearization of the form $h_t \approx C_{11}(\theta)h_{xx}$. (a) Compared to existing models, which all exhibit a band of unstable angles above some transition angle, the swelling mechanism is stable for all angles of incidence. (b) As swelling is added at increasing ratios to the existing stability profile, the critical angle shifts to higher angles, and eventually may vanish entirely. (Here, 'ratio' indicates the relative magnitude of the swelling mechanism compared to the existing profile, and the resulting sums are scaled by the value of $C_{11}(0)$.)

5.1.2. Ne^+,$Ar^+ \rightarrow$ Ge below 2000 eV. We now turn to the irradiation of Ge by various ions at similar energies, as reported by Teichmann *et al* [34]. Surprisingly, for Ne^+ and Ar^+ ions, no pattern formation is observed at any angle of incidence in this energy range (at least, no angle less than 75°, which was the maximum angle studied). This observation is consistent with our model if we assume that Ge experiences much more swelling than Si under similar irradiation conditions. And in fact, this is precisely the case—Ge can be shown to readily double in volume [36, 45] due to the stabilization of vacancies and their accumulation into voids [46, 47].

5.1.3. Kr^+,$Xe^+ \rightarrow$ Ge below 2000 eV. Teichmann *et al* also studied irradiation of Ge by the heavier ions Kr^+ and Xe^+ [34], where 'standard' patterning behavior is observed, with two important differences. First, the transition angles are much higher than for the $Ar^+ \rightarrow$ Si system (in the vicinity of 65°). Second, in a series of experiments at 65°, strong ripples were osbseved at 400 eV, weaker ripples at 800 and 1200 eV, and no ripples at 2000 eV. Repeating these experiments at 75°, the authors observed ripples at all energies, and therefore concluded that the transition angle had increased with increasing ion energy. These behaviors are also consistent with our findings, if we assume that the relevant strength of swelling increases with ion energy; indeed, this is suggested by the experiments of Böttger *et al* [48].

5.1.4. $Ar^+ \rightarrow$ Si above 2000 eV. Finally, we consider some observations for the $Ar^+ \rightarrow$ Si system at higher energies between 650 eV and 10 keV, as reported by Hofsäss *et al* [35]. These authors performed a series of experiments at 65°, observing strong patterns at 650 eV, weaker patterns at 1 keV and 1.3 keV, and essentially no patterns between 3 keV and 10 keV. Being essentially identical to the results in [34] for Kr^+ and Xe^+ on Ge, these observations are also consistent with our findings, under the assumptions described above.

5.2. Directions for future work

5.2.1. Transition angles: vanished or moved? The observations above naturally suggest the question of whether a transition from flat to rippled surfaces was, in fact, entirely suppressed in any of the above systems, or whether it simply moved to a higher angle of incidence. For the Kr^+,$Xe^+ \rightarrow$ Ge system, when increasing energies caused ripples to vanish at 65°, Teichmann *et al* repeated their experiments at 75°, confirming that ripples persist at all energies for this higher incidence angle. However, for the Ne^+,$Ar^+ \rightarrow$ Ge system, when ripples were not observed at any angle below 75°, those authors did not report further experiments at even higher angles. Similarly, for the $Ar^+ \rightarrow$ Si system, when increasing energies caused ripples to vanish at 65°, Hofsäss *et al* did not report further experiments at higher angles[2] [35]. We therefore consider these regions of parameter space to be of high interest for continued study.

5.2.2. Model refinements: swelling saturation. The simple model of swelling represented by equation (3) has the advantage of mathematical simplicity, and generalization across different atomic-level volumization mechanisms. One disadvantage is that it does not contain a saturation mechanism. This was not a problem in [44] when the rate of swelling was assumed to be small. For larger swelling rates, this may or may not need refinement. We note that material parcels undergo swelling only until they are sputtered away at the top surface. Therefore, if the 'dwell time' $\tau_{\text{dwell}} = \frac{h_0}{V}$ needed to sputter away one film depth's worth of material is less than the time τ_{sat} at which

[2] We note that in [35], Hofsäss *et al* argued that ripples *could not form* for any angle at these energies, based on simulations using a a modified version of the Crater Function Framework proposed in [49, 50]. However, this reasoning assumes prompt erosive and redistributive effects alone determine patterning behavior, which is inconsistent with recent studies of ion-induced stresses [24–29]. Moreover, as we have noted elsewhere [30], several of the proposed modifications do not appear to be mathematically justified.

the stress would saturate without sputtering, then the linear approximation in equation (3) remains reasonable. This seems to be the case at least for the 'reference' system of $Ar^+ \rightarrow Si$ below 1 keV [21]. If $\tau_{FD} > \tau_{SS}$, a refinement would be needed. We defer such refinement to future work.

5.2.3. Energy dependence: a complex space. The energy dependence of patterning behavior is highly complex. For instance, in the $Ar^+ \rightarrow Si$ system [35], identify three distinct energy regimes. In 'Region 1' (below 1 keV), patterns are readily formed at angles above 45 degrees [31]. In 'Region 2' (from 1 keV to 20 keV), patterns are less easily formed, with a higher transition angle that can exceed 65 degrees, and may potentially vanish entirely [35]. Finally, in 'Region 3' (above 20 keV), patterns again readily formed, and the transition angle decreases again, potentially as low as 30 degrees at an energy of 40 keV [51]. So, although we have suggested that an energy-dependent swelling may explain the transition from 'Region 1' to 'Region 2' type behavior in some relevant systems [34, 35], a simple extrapolation of this trend to all energies is obviously insufficient.

There are several reasons to expect that a more nuanced approach should be needed. First, as shown in [44], the 'dwell time' τ_{dwell} introduced above has a minimum value at around 1–2 keV. Above this energy, it increases steadily, doubling by 10 keV, and doubling again by 30 keV. As material spends increasing amounts of time in the amorphous film prior to sputtering, we may expect the importance of bulk physics (such as stress-driven viscous flow [24, 25, 27, 28]) to increase relative to surface physics (such as surface sputtering and redistribution [5–7, 9–11, 16, 17]). An increasing dwell time may also necessitate the inclusion of a saturation mechanism as just described, which in turn, could limit the suppressive effect of swelling as energies continue to increase. Second, the fundamental physics of ion/solid interactions are changing at these energy levels. Ions moving through solids undergo both nuclear and electronic stopping [52], and above a certain energy, electronic stopping becomes dominant. Indeed, for the $Ar \rightarrow Si$ sytem, nuclear stopping reaches a peak at around 20 keV [53]—exactly the boundary between 'Region 2' and 'Region 3' as described by [35]. In short, because the underlying physics of the system are changing, it is not unreasonable that trends in the relative magnitude of parameters might change direction in this region. Indeed, ion-solid interactions at higher energies have previously been described using entirely different modeling approaches (see e.g. [19, 54–62]). Much more work is needed, but we hope this contribution motivates future studies.

6. Conclusion

As described above, past work from our group [44] has shown that a simple mathematical model of radiation-induced swelling, a mechanism historically neglected in theoretical treatments of ion-induced nanopatterning, is unconditionally stabilizing. This may, in principle, provide a means of explaining the disappearance of ion-induced nanopatterns observed for certain ion/target/energy combinations [34, 35]. However, an important limitation to the previous work was its restriction to the limit of small swelling rates. While the analysis showing unconditional stability of the swelling mechanism used the assumption of a small swelling rate (A) in order to render the governing equations analytically solvable, the actual suppression of pattern formation observed experimentally would only be expected to appear for relatively large swelling rates. Hence, some means of 'bridging the gap' between these two regimes was needed. This work has provided such a bridge by employing a numerical study of the linear stability equations, an approach not commonly seen but broadly applicable to other systems.

The present work overcomes the previous limitations on parameter A, successfully bridging the gap: the stabilization of observed wavelengths is not a transient artifact of the small swelling rate assumption made originally, but is, rather, due to the nature of the swelling mechanism itself. Indeed, there are very strong similarities between the behavior associated with small swelling rates, and that associated with even very large swelling rates. In fact, at normal incidence, the behavior over different wavenumbers and swelling rates is very nearly separable, and we have derived a simple prefactor function that scales the small-swelling result into the arbitrary-swelling regime. The persistence of these stabilization effects for all swelling rates strengthens the argument for adding a swelling-type mechanism to models of nanopattern formation, and the great similarities in the dispersion relation across all swelling rates suggests that the small-swelling limit obtained in [44] is an adequate approximation to the full mechanism.

Having verified the behavior of the swelling mechanism for arbitrary swelling rates, we also made some testable predictions of its effect on experimental systems. The most important of these is that *swelling should increase the transition angle between flat and patterned surfaces*, potentially eliminating patterns entirely if it is strong enough. Combined with the knowledge that irradiated Ge readily swells to almost double its initial volume [45], this prediction would explain the observations of Teichmann *et al* [34], who observed no ripples in the $Ne^+ \rightarrow Ge$ and $Ar^+ \rightarrow Ge$ systems at any incidence angle, and ripples only at high incidence angles in the $Kr^+ \rightarrow Ge$ and $Xe^+ \rightarrow Ge$ systems. If we further predict that swelling increases with ion energy in this energy range, we can additionally explain the increasing transition angles observed by Teichmann *et al* in $Kr^+ \rightarrow Ge$ between 400 eV and 2000 eV, and by Hofsäss *et al* in $Ar^+ \rightarrow Si$ between 650 eV and 3000 eV [34, 35].

These theoretical advancements, and associated predictions, highlight a paucity of experimental measurements needed to compare the relative magnitudes of active mechanisms in ion-irradiated solids. For instance, to quantify the discussion presented in section 5.1, we would need simultaneous measurements of both the (isotropic) swelling rate (isotropic stress) *and* the (deviatoric) stress-driven viscous flow rate, across a wide range of energies. Although both swelling

and stress can be measured independently, we are aware of only one limited study that attempts to distinguish between these two quantities, by collecting *angle-dependent* measurements of cantilever curvature [22]. That study does appear to suggest the presence of both effects even at low energies (250 eV Ar^+ on Si), further indicating that the inclusion of swelling effects may be necessary to obtain the quantitatively-accurate 'predictive model' so long sought in this field [30]. More experimental work in this area will be crucial component of this ongoing pursuit.

Data availability statement

The data that support the findings of this study are available upon reasonable request from the authors.

Acknowledgment

We gratefully acknowledge support from the National Science Foundation through DMS-1840260.

Appendix. Long-wave limit, arbitrary swelling rate

As a simple first step in determining whether the swelling mechanism continues to produce a regime of stabilizing wave numbers for arbitrary swelling rates, we consider an alternate linearization of equations (15)–(25), in small wavenumber Q, rather than in small swelling rate A, in order to understand the long-wave behavior of the swelling mechanism in general. We expand equations (15)–(25) in a standard asymptotic series for small Q by applying the following set of ansatzes

$$\rho_1(z)=\sum_{i=0}^{\infty}Q^i\rho_{1i}(z);\quad u_1(z)=\sum_{i=0}^{\infty}Q^i u_{1i}(z);$$
$$w_1(z)=\sum_{i=0}^{\infty}Q^i w_{1i}(z);\quad p_1(z)=\sum_{i=0}^{\infty}Q^i p_{1i}(z);$$
$$a_1(z)=\sum_{i=0}^{\infty}Q^i a_{1i}(z);\quad \Sigma=\sum_{i=0}^{\infty}Q^i\Sigma_i,$$

deriving new sets of differential equations in the coefficients and solving them. The results will then provide good approximations to the $\rho_1, u_1, w_1, p_1, a_1$ and Σ that we seek when $Q\approx 0$. Although the system, in principle, will admit multiple solutions for Σ, we are usually concerned only with the most positive branch, since this will determine the pattern formation that is actually observed. This suggests that we should begin the analysis by seeking perturbation solutions near $\Sigma_0=0$. We now provide a brief summary of the solution up to $O(Q^2)$ with this assumption about Σ_0. We will refer to this as the *'main branch'*.

At O(1)

The $i=0$ term may be computed by setting $Q\to 0, \Sigma_0\to 0$ for equations (9)–(19). This leads to the bulk equations

$$\frac{-A}{\psi^3}w_{10}+\frac{w_{10}'}{\psi}+\psi\rho_{10}'+\frac{A}{\psi}\rho_{10}=0 \tag{38}$$

$$\psi a_{10}'+\frac{A}{\psi}w_{10}=0 \tag{39}$$

$$\psi\rho_{10}+\frac{a_{10}}{\psi}=0 \tag{40}$$

$$u_{10}''=0 \tag{41}$$

$$2w_{10}''=p_{10}', \tag{42}$$

with

$$a_{10}=-h_{11}A \tag{43}$$

$$u_{10}=0 \tag{44}$$

$$w_{10}=-h_{11}A \tag{45}$$

at $z=0$, and

$$w_{10}=-(1+2A)\rho_{10} \tag{46}$$

$$u_{10}'=0 \tag{47}$$

$$-p_{10}+2w_{10}'=0 \tag{48}$$

at $z=1$. It is clear that u_{10} is at most a polynomial. From equations (39) and (40), we may obtain a_{10} in terms of ρ_{10}, and then w_{10} is known in terms of the ρ_{10} by substitution. These relationships may be applied to (38) to obtain a differential equation purely in terms of ρ_{10}, which is readily solvable. Having obtained ρ_{10}, we know a_{10} from (11) and w_{10} from having already identified w_{10} in terms of a_{10}. Then p_{10} may be obtained from (42), and the boundary conditions are easy to match. We obtain the following solution set at $O(1)$ for the main branch:

$$w_{10}=\frac{-Ah_{11}}{\sqrt{1+2Az}} \tag{49}$$

$$u_{10}=0 \tag{50}$$

$$p_{10}=\frac{2A^2\,h_{11}}{(1+2Az)^{3/2}} \tag{51}$$

$$\rho_{10} = \frac{Ah_{11}}{(1+2Az)^{3/2}} \tag{52}$$

$$a_{10} = \frac{-Ah_{11}}{\sqrt{1+2Az}} \tag{53}$$

$$\Sigma_0 = 0. \tag{54}$$

At O(Q)

We obtain the bulk equations

$$\Sigma_1\rho_{10} - \frac{A}{\psi^3}w_{11} + \frac{w'_{11}}{\psi} + \psi\rho'_{11} + \frac{A\rho_{11}}{\psi} = 0 \tag{55}$$

$$\Sigma_1 a_{10} + \psi a'_{11} + \frac{Aw_{11}}{\psi} = 0 \tag{56}$$

$$\psi\rho_{11} + \frac{a_{11}}{\psi} = 0 \tag{57}$$

$$u''_{11} + iw'_{10} = ip_{10} \tag{58}$$

$$p'_{11} = 2w''_{11} \tag{59}$$

with boundary conditions at $z = 0$:

$$a_{11} = 0 \tag{60}$$

$$u_{11} = 0 \tag{61}$$

$$w_{11} = 0 \tag{62}$$

and boundary conditions at $z = 1$:

$$w_{11} = \Sigma_1 h_{21} - (1+2A)\rho_{11} \tag{63}$$

$$u'_{11} + iw_{10} = \frac{-2iAh_{21}}{\sqrt{1+2A}} \tag{64}$$

$$-p_{11} + 2w'_{11} = 0 \tag{65}$$

from which we obtain

$$a_{11} = w_{11} = \rho_{11} = p_{11} = \Sigma_1 = 0 \tag{66}$$

$$u_{11} = i\left(h_{11} + \frac{2A(h_{11}-h_{21})z}{\sqrt{1+2A}} - h_{11}\sqrt{1+2Az}\right). \tag{67}$$

As before, the primary 'trick' is in exploiting the linearized equation of state. Here, we use equation (59) to determine that p_{11} is a constant, and (58) can be integrated twice to provide the u_{11} in terms of the $O(1)$ results. Equation (57) gives a relationship between a_{11} and ρ_{11} which can be substituted into (56) to obtain w_{11} in terms of $O(1)$ results and ρ_{11}. This may be substituted into (55) to arrive at a differential equation in terms of ρ_{11} which is solvable in closed form. We may then back-substitute to obtain the solutions for all other quantities.

At $O(Q^2)$

We obtain the bulk equations

$$\Sigma_2\rho_{10} + \Sigma_1\rho_{11} - \frac{Aw_{12}}{\psi^3} + \frac{1}{\psi}(iu_{11} + w'_{12}) + \psi\rho'_{12} + \frac{A}{\psi}\rho_{12} = 0 \tag{68}$$

$$\Sigma_2 a_{10} + \Sigma_1 a_{11} + \psi a'_{12} + \frac{Aw_{12}}{\psi} = 0 \tag{69}$$

$$\psi\rho_{12} + \frac{a_{12}}{\psi} = 0 \tag{70}$$

$$-2u_{10} + u''_{12} + iw'_{11} = ip_{11} \tag{71}$$

$$-w_{10} + 2w''_{12} + iu'_{11} = p'_{12} \tag{72}$$

with boundary conditions at $z = 0$:

$$a_{12} = 0 \tag{73}$$

$$u_{12} = 0 \tag{74}$$

$$w_{12} = 0 \tag{75}$$

and boundary conditions at $z = 1$:

$$w_{12} = h_{21}\Sigma_{12} - (1+2A)\rho_{12} \tag{76}$$

$$u'_{12} + iw_{11} = 0 \tag{77}$$

$$-p_{12} + 2\,w'_{12} = 0 \tag{78}$$

from which we may finally obtain Σ_2. The solution method is similar to the first two orders of Q. From (72) we obtain p_{12} in terms of known quantities. Equation (71) may be integrated twice to obtain u_{12} in terms of known quantities. Then we may solve for a_{12} in terms of ρ_{12} and known quantities using (71). Using (70) as before, we obtain w_{12} in terms of ρ_{21} and known quantities, which may be substituted into (68) to arrive at a differential equation that is solvable for ρ_{21}, and the other quantities may be obtained by back-substitution. The boundary conditions, as before, are easy to handle although the calculations are somewhat lengthy. It is at $O(Q^2)$ that we obtain our first non-zero solution in the small-Q approximation of Σ.

Results

Therefore we have in the long-wave limit, to leading order in Q,

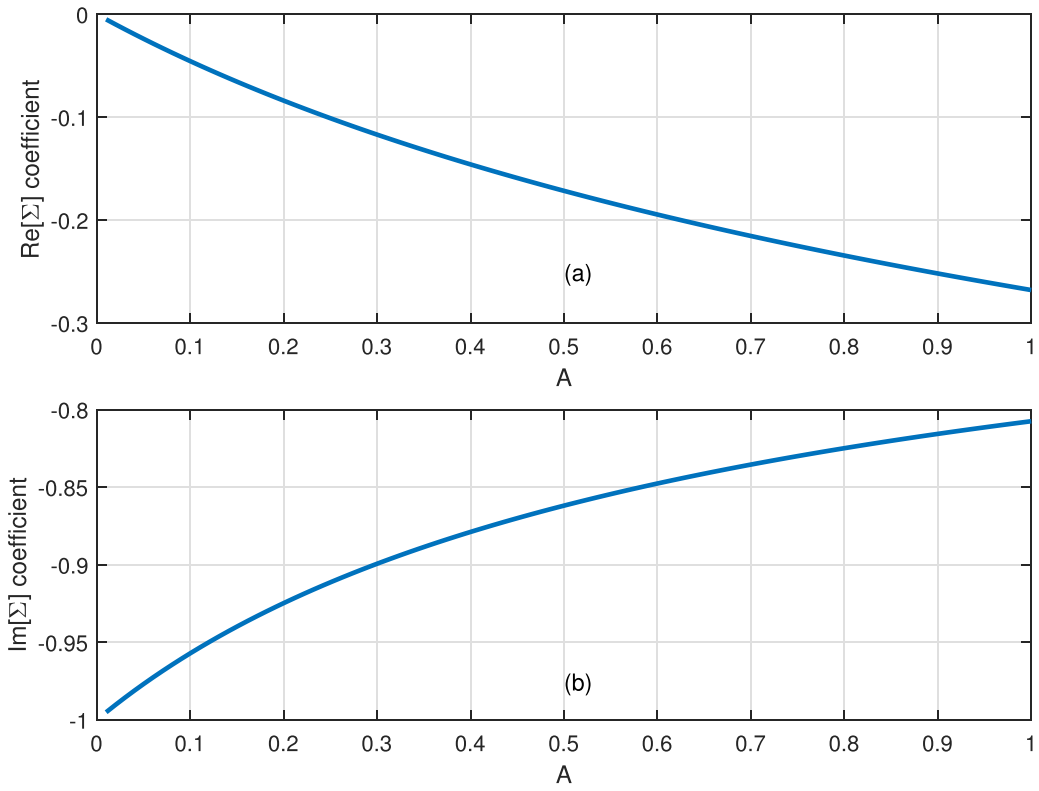

Figure 9. The A-dependent, angle-independent coefficient from (a) the real part and (b) the imaginary part of the long-wave dispersion relation, from equations (80) to (81).

$$\Sigma \approx \frac{Q^2(2(-2A^2+A-\sqrt{2A+1}+1)h_{21}+5(\sqrt{2A+1}-1)h_{11}+A(-2A+6\sqrt{2A+1}-11)h_{11})}{3A((2A+1)h_{11}+\sqrt{2A+1}(h_{21}-h_{11}))} \tag{79}$$

which is proportional to $-Q^2$, and this gives us a good approximation of the main branch of the dispersion relation for small wave numbers. As described above, the dependence on incidence angle can be explored by re-scaling the film depth, wave number, and linearized interface perturbations (h_0, Q, h_{11}, h_{21} respectively) using equations (32)–(34). Dividing numerator and denominator by h_{21}, applying those substitutions, and then performing a Taylor expansion for $Q \approx 0$, we deduce the angle- and swelling rate-dependent long-wave solution

$$\mathrm{Re}[\Sigma(Q,\theta;A)] \approx \frac{\left(-A+\sqrt{2A+1}-1\right)Q^2\cos^2(\theta)}{A} \tag{80}$$

and

$$\mathrm{Im}[\Sigma(Q,\theta;A)] \approx -\frac{\left(\sqrt{2A+1}+A\left(2\sqrt{2A+1}-3\right)-1\right)Q^3\sin(\theta)\cos^3(\theta)}{3A\sqrt{2A+1}} \tag{81}$$

which are much simpler forms accounting for the growth and translation, respectively, of long-wave perturbations. We note that a second Taylor expansion in A for $A \approx 0$ for (80) and (81) reproduces the result given in [44],

$$\mathrm{Re}[\Sigma(Q,\theta,0)] \approx -\frac{1}{2}AQ^2\cos^2(\theta). \tag{82}$$

We note that for $\theta = 0$, the imaginary part drops out of our result entirely, consistent with previous results at normal incidence. It is clear that for all values of A, small wave numbers are stable, reflecting that the swelling mechanism induces a pocket of stability for some range of long wave numbers at all angles of incidence. Hence the stabilizing effect of the swelling mechanism is established for arbitrary swelling rates, angle of incidence and *at least* long waves. For interest, we have plotted the A-dependent coefficients of equations (80) and (81) above in figure 2.

ORCID iD

Tyler Evans https://orcid.org/0000-0001-7812-2479

References

[1] Navez M, Chaperot D and Sella C 1962 Microscopie electronique-etude de lattaque du verre par bombardement ionique *C. R. Hebd. Seances Acad. Sci.* **254** 240

[2] Facsko S, Dekorsy T, Koerdt C, Trappe C, Kurz H, Vogt A and Hartnagel H L 1999 Formation of ordered nanoscale semiconductor dots by ion sputtering *Science* **285** 1551–3

[3] Frost F, Ziberi B, Schindler A and Rauschenbach B 2008 Surface engineering with ion beams: from self-organized nanostructures to ultra-smooth surfaces *Appl. Phys.* A **91** 551–9

[4] Chan W L and Chason E 2007 Making waves: kinetic processes controlling surface evolution during low energy ion sputtering *J. Appl. Phys.* **101** 121301

[5] Sigmund P 1969 Theory of sputtering. I. Sputtering yield of amorphous and polycrystalline targets *Phys. Rev.* **184** 383–416

[6] Sigmund P 1973 A mechanism of surface micro-roughening by ion bombardment *J. Mater. Sci.* **8** 1545–53

[7] Bradley R M and Harper J M 1988 Theory of ripple topography induced by ion bombardment *J. Vac. Sci. Technol.* **6** 2390–5

[8] Makeev M A, Cuerno R and Barabási A-L 2002 Morphology of ion-sputtered surfaces *Nucl. Instrum. Methods Phys. Res.* B **197** 185–227

[9] Carter G and Vishnyakov V 1996 Roughening and ripple instabilities on ion-bombarded Si *Phys. Rev.* B **54** 17647–53

[10] Moseler M, Gumbsch P, Casiraghi C, Ferrari A C and Robertson J 2005 The ultrasmoothness of diamond-like carbon surfaces *Science* **309** 1545–8

[11] Davidovitch B, Aziz M J and Brenner M P 2009 Linear dynamics of ion sputtered surfaces: instability, stability and bifurcations *J. Phys.: Condens. Matter* **21** 224019

[12] Madi C S, Anzenberg E, Ludwig K F Jr and Aziz M J 2011 Mass redistribution causes the structural richness of ion-irradiated surfaces *Phys. Rev. Lett.* **106** 066101

[13] Kalyanasundaram N, Ghazisaeidi M, Freund J B and Johnson H T 2008 Single impact crater functions for ion bombardment of silicon *Appl. Phys. Lett.* **92** 131909

[14] Kalyanasundaram N, Freund J B and Johnson H T 2009 A multiscale crater function model for ion-induced pattern formation in silicon *J. Phys.: Condens. Matter* **21** 224018

[15] Norris S A, Brenner M P and Aziz M J 2009 From crater functions to partial differential equations: a new approach to ion bombardment induced nonequilibrium pattern formation *J. Phys.: Condens. Matter* **21** 224017

[16] Norris S A, Samela J, Bukonte L, Backman M, Nordlund D F K, Madi C, Brenner M and Aziz M 2011 Molecular dynamics of single-particle impacts predicts phase diagrams for large scale pattern formation *Nat. Commun.* **2** 276

[17] Harrison M P and Bradley R M 2014 Crater function approach to ion-induced nanoscale pattern formation: craters for flat surfaces are insufficient *Phys. Rev.* B **89** 245401

[18] Umbach C C, Headrick R L and Chang K-C 2001 Spontaneous nanoscale corrugation of ion-eroded SiO_2: the role of ion-irradiation-enhanced viscous flow *Phys. Rev. Lett.* **87** 246104

[19] Brongersma M L, Snoeks E, van Dillen T and Polman A 2000 Origin of MeV ion irradiation-induced stress changes in SiO_2 *J. Appl. Phys.* **88** 59–64

[20] Chan W L and Chason E 2008 Stress evolution and defect diffusion in Cu during low energy ion irradiation: experiments and modeling *J. Vac. Sci. Technol.* A **26** 44

[21] Madi C S 2011 Linear stability and instability patterns in ion bombarded silicon surfaces *PhD Dissertation* Harvard University

[22] Perkinson J C 2017 *PhD Dissertation* Harvard University

[23] Ishii Y, Madi C, Aziz M J and Chason E 2014 Stress evolution in Si during low-energy ion bombardment *J. Mater. Res.* **29** 2942–8

[24] Castro M and Cuerno R 2012 Hydrodynamic approach to surface pattern formation by ion beams *Appl. Surf. Sci.* **258** 4171–8

[25] Castro M, Gago R, Vázquez L, Muñoz-García J and Cuerno R 2012 Stress-induced solid flow drives surface nanopatterning of silicon by ion-beam irradiation *Phys. Rev.* B **86** 214107

[26] Norris S A 2012 Stability analysis of a viscoelastic model for ion-irradiated silicon *Phys. Rev.* B **85** 155325

[27] Norris S A 2012 Stress-induced patterns in ion-irradiated silicon: model based on anisotropic plastic flow *Phys. Rev.* B **86** 235405

[28] Moreno-Barrado A, Castro M, Gago R, Vãzquez L, Muñoz-García J, Redondo-Cubero R, Galiana B, Ballesteros C and Cuerno R 2015 Nonuniversality due to inhomogeneous stress in semiconductor surface nanopatterning by low-energy ion-beam irradiation *Phys. Rev.* B **91** 155303

[29] Norris S A, Perkinson J C, Mokhtarzadeh M, Anzenberg E, Aziz M J and Ludwig K F Jr 2017 Distinguishing physical mechanisms using GISAXS experiments and linear theory: the importance of high wavenumbers *Sci. Rep.* **7** 2016

[30] Norris S A and Aziz M J 2019 Ion-induced nanopatterning of silicon: toward a predictive model *Appl. Phys. Rev.* **6** 011311

[31] Madi C S, Davidovitch B P, George H B, Norris S A, Brenner M P and Aziz M J 2008 Multiple bifurcation types and the linear dynamics of ion sputtered surfaces *Phys. Rev. Lett.* **101** 246102

[32] Madi C S, George H B and Aziz M J 2009 Linear stability and instability patterns in ion-sputtered silicon *J. Phys.: Condens. Matter* **21** 224010

[33] Madi C S and Aziz M J 2012 Multiple scattering causes the low energy-low angle constant wavelength bifurcation of argon ion bombarded silicon surfaces *Appl. Surf. Sci.* **258** 4112–5

[34] Teichmann M, Lorbeer J, Ziberi B, Frost F and Rauschenbach B 2013 Pattern formation on Ge by low energy ion beam erosion *New J. Phys.* **15** 103029

[35] Hofsäss H, Bobes O and Zhang K 2016 Argon ion beam induced surface pattern formation on Si *J. Appl. Phys.* **119** 035302

[36] Wilson I 1982 The effects of self-ion bombardment (30–500 keV) on the surface topography of single-crystal germanium *J. Appl. Phys.* **53** 1698

[37] Appleton B, Holland O, Narayan J, Schow O E III, Williams J, Short K and Lawson E 1982 Characterization of damage in ion implanted Ge *Appl. Phys. Lett.* **41** 711

[38] Holland O, Appleton B and Narayan J 1983 Ion implantation damage and annealing in germanium *J. Appl. Phys.* **54** 2295

[39] Jafri Z, Jeynes C, Webb R and Wilson I 1989 Observation of swelling and sputtering of a silicon target under argon ion irradiation using a double marker technique *Vacuum* **39** 1119–21

[40] McHargue C and Williams J 1993 Ion implantation effects in silicon carbide *Nucl. Instrum. Methods Phys. Res.* B **80–81** 889–94

[41] Tamulevicius S, Pozela I and Andrulevicius M 1996 A simple model of radiation swelling in silicon *Mater. Sci. Eng.* B **40** 141–6

[42] Giri P, Raineri V, Franzo G and Rimini E 2001 Mechanism of swelling in low-energy ion-irradiated silicon *Phys. Rev.* B **65** 012110

[43] Chini T K, Okuyama F, Tanemura M and Nordlund K 2003 Structural investigation of keV Ar-ion-induced surface

ripples in Si by cross-sectional transmission electron microscopy *Phys. Rev.* B **67** 205403
[44] Swenson J M and Norris S A 2018 Swelling as a stabilizing mechanism in irradiated thin films *J. Phys.: Condens. Matter* **30** 304003
[45] Wang L and Birtcher R 1989 Radiation-induced formation of cavities in amorphous germanium *Appl. Phys. Lett.* **55** 2494
[46] Watkins G D 2000 Intrinsic defects in silicon *Mater. Sci. Semicond. Process.* **3** 227–35
[47] Edler T and Mayr S 2007 Mechanisms of stress generation during bombardment of Ge with keV ions: experiments and molecular dynamics simulations *New J. Phys.* **9** 325
[48] Böttger R, Heinig K-H, Bischoff L, Liedke B and Facsko S 2013 From holes to sponge at irradiated ge surfaces with increasing ion energy—an effect of defect kinetics? *Appl. Phys.* A **113** 53–59
[49] Hofsäss H 2014 Surface instability and pattern formation by ion-induced erosion and mass redistribution *Appl. Phys.* A **114** 401–22
[50] Hofsäss H 2015 Model for roughening and ripple instability due to ion-induced mass redistribution [addendum to H. Hofsäss, Appl. Phys. A 114 (2014) 401, "Surface instability and pattern formation by ion-induced erosion and mass redistribution"] *Appl. Phys.* A **119** 687–95
[51] Carter G, Nobes M, Paton F and Williams J 1977 Ion bombardment induced ripple topography on amorphous solids *Radiat. Eff.* **33** 65–73
[52] Ziegler J F, Biersack J P and Littmark U 1985 *The Stopping and Range of Ions in Matter* (New York: Pergamon)
[53] Liedke B 2011 Ion beam processing of surfaces and interfaces: modeling and atomistic simulations *PhD Dissertation* Helmholtz Zentrum Dresden Rossendorf
[54] Volkert C A 1991 Stress and plastic flow in silicon during amorphization by ion bombardment *J. Appl. Phys.* **70** 3521
[55] Trinkaus H and Ryazanov A I 1995 Viscoelastic model for the plastic flow of amorphous solids under energetic ion bombardment *Phys. Rev. Lett.* **75** 5072–5
[56] Snoeks E, Weber T, Cacciato A and Polman A 1995 MeV ion irradiation-induced creation and relaxation of mechanical stress in silica *J. Appl. Phys.* **78** 4723
[57] Trinkaus H 1998 Dynamics of viscoelastic flow in ion tracks: origin of plastic deformation of amorphous materials *Nucl. Instrum. Methods Phys. Res.* B **146** 204–16
[58] van Dillen T, Polman A, Fukarek W and van Blaaderen A 2001 Energy-dependent anisotropic deformation of colloidal silica particles under MeV Au irradiation *Appl. Phys. Lett.* **78** 910–2
[59] van Dillen T, Polman A, van Kats C M and van Blaaderen A 2003 Ion beam-induced anisotropic plastic deformation at 300 keV *Appl. Phys. Lett.* **83** 4315–7
[60] van Dillen T, Polman A, Onck P R and van der Giessen E 2005 Anisotropic plastic deformation by viscous flow in ion tracks *Phys. Rev.* B **71** 024103
[61] Mayr S G and Averback R S 2005 Ion-irradiation-induced stresses and swelling in amorphous Ge thin films *Phys. Rev.* B **71** 134102
[62] Otani K, Chen X, Hutchinson J W, Chervinsky J F and Aziz M J 2006 Three-dimensional morphology evolution of SiO_2 patterned films under MeV ion irradiation *J. Appl. Phys.* **100** 023535